Title: Myelin contributes to microstructural growth in human sensory cortex during early infancy

Authors: Mona *Rosenke[1]†, Vaidehi S. Natu[1]†*, Hua Wu[1], Francesca R. Querdasi[1], Holly Kular[1], Nancy Lopez-Alvarez[1], Mareike Grotheer[1,2,3], Shai Berman[4], Aviv A. Mezer[4], Kalanit Grill-Spector[1,5,6]*

Affiliations:

[1]Department of Psychology, Stanford University, Stanford, CA 94305, USA

[2]Department of Psychology, University of Marburg, Marburg 35039, Germany

[3]Center for Mind, Brain and Behavior - CMBB, Marburg 35032, Germany

[4]Edmond and Lily Safra Center for Brain Sciences, Hebrew University of Jerusalem, Jerusalem 91904, Israel

[5]Neurosciences Program, Stanford University, Stanford, CA 94305, USA

[6]Wu Tsai Neurosciences Institute, Stanford University, Stanford, CA 94305, USA

†These authors have contributed equally to this work.

Correspondence to: *vnatu@stanford.edu*

Short title: Cortical myelination in infancy

Abstract: The infant brain undergoes rapid physical changes after birth. However, how cortex develops remains unknown. Using *in vivo* biomarkers of tissue microstructure, we find that infants' sensory-motor cortices undergo profound microstructural growth during the first six months of life. Using visual cortex as a model system, we find hierarchical microstructural growth: higher-level visual areas have less mature tissue at birth than earlier visual areas but grow at faster rates. Comparison of postnatal to prenatal gene expression data suggests that myelination and synaptic processes are dominant contributors to postnatal development. These data suggest a rethinking of developmental hypotheses and highlight the significance of cortical myelination in the development of brain function. Our findings have important implications for diagnosis of neurodevelopmental disorders and delays affecting life-long outcomes.

One Sentence Summary: Infant sensory cortices mature hierarchically as earlier cortical areas have more myelin and synapses but grow slower.

The establishment of neural circuitry during early infancy is critical for developing visual, auditory, and motor functions. However, how cortical microstructure in infants develops to support this neural circuitry remains unknown. While many studies have documented increases in cortical volume during the first 2 years of life (*1*, *2*) few studies investigated microstructural development in infants' cortex. *In vivo* measurements of microstrucural development in humans are critical because humans undergo a protracted development and have different anatomy and microstructure compared to other species. Prior investigations in humans have examined a handful of areas (*3*, *4*) (primary visual and motor cortices (V1, M1) and prefrontal cortex (*5*), or coarse patterns of development spanning lobes (*6–8*). *Ex vivo* studies of infant V1 and M1 found myelination (*4*), synaptogenesis (*3*) and dendritic spine growth (*5*) even as the number of neurons remains largely stable and irrelevant axons and synapses are pruned (*3*). Nonetheless, the scope of *ex vivo* studies is limited because they are cross-sectional and include atypical brain samples. This leaves glaring gaps in knowledge regarding the origin, sequence, and rate of microstructural tissue development in sensory cortex of typically developing infants.

To fill this gap, we leveraged recent advancements in quantitative magnetic resonance imaging (qMRI) (*9*, *10*) and diffusion MRI (dMRI) (*11*) to develop novel *in vivo* methodologies that measure longitudinal cortical microstructure development during the first 6 months of human life. Specifically, quantitative measurements of proton relaxation time (T_1) from qMRI and mean diffusivity (MD) from dMRI allow quantification of brain tissue related to the neuropil and myelin at the voxel level (1-2mm), both within and across individuals over time (*12*, *13*). Critically, these measurements are metric, have units, and can disambiguate developmental hypotheses to test if cortical microstructure: (1) proliferates, predicting decreases in T_1 and MD with age or (2) prunes, predicting increases in T_1 and MD. We tested these hypotheses in (i) primary sensory-motor areas to relate our measurements to prior *ex vivo* research and (ii) across the visual system, as it contains two well-agreed upon processing hierarchies (*14*), which offers an exciting opportunity to study microstructural development across an entire sensory hierarchy for the first time.

Anatomical MRI, qMRI, and dMRI data were collected in 13 full-term infants (6 female) who were scanned during normal sleep at 0 months [8-37 days], 3 months [78-106 days], and 6 months [167-195 days] (10 infants per timepoint, 7 infants scanned longitudinally at all timepoints, **Fig. S1** and Materials and Methods). For quality assurance, we monitored in real-time each infant's motion via an infrared camera, assessed brain images immediately after acquisition, and repeated scans with motion artifacts. From anatomical MRIs, we generated a cortical surface for each infant and timepoint (**Fig. S1**). This enabled analysis of T_1 and MD across cortex in native brain space. Finally, cortical-based alignment was used to delineate known cortical areas (*15*, *16*) in each infant's brain to achieve the most precise measurements.

Longitudinal cortical T_1 maps reveal that T_1 decreases from birth to 6 months. This decrease is heterogenous across cortex (example infant: **Fig. 1A;** all infants: **Fig. S2**). E.g., at 3 months, occipital cortex and the central sulcus have lower T_1 (black arrows in **Fig. 1A**) than parietal and frontal cortices (red arrows in **Figs. 1A**, **S2**) even though all of cortex at 3 months has lower T_1 than that at birth.

Next, we quantitatively measured T_1 and MD in four primary sensory-motor areas (*16*): visual (V1), auditory (A1), somatosensory (S1), and motor (M1) (**Fig. 1B**), which overlap the cortical expanse showing rapid development. We found a systematic decrease in the distribution of T_1 values from birth to 6 months in all primary areas (**Fig. 1C**). Across all primary sensory-motor regions, mean T_1 substantially decreased from 2.03s ±0.07s (mean (M)±standard deviation (SD)) in newborns, to 1.87s ± 0.08s at 3 months, to 1.74s ± 0.06s at 6 months. To quantify the rate of microstructural development, we fit linear mixed models (LMMs) relating mean T_1 [s] to age [days] with infants as random factor. Results revealed a significant linear decrease in mean T_1 across all areas (right hemisphere: **Fig. 1D,** left hemisphere: **Fig. S3A**, slopes: -1.3 to -2 [ms/day]; *P*s<10^{-7}, **Table S2**-all stats). The slopes of LMMs [ms/day], which represent rate of T_1 development, indicate similar rates of T_1 decrease across primary areas. However, intercepts [s], which represent estimated T_1 at birth, reveal that V1 has higher T_1 at birth, suggesting denser microstructure at birth than other primary areas. Analysis of MD in these areas revealed similar significant, linear decreases from 0 to 6 months (right hemisphere: **Figs. 1E, 1F**, left hemisphere: **Fig. S4**, LMM slopes: -9.36x10^{-7} to -1.01x10^{-6} [s/day]; *P*s<0.001, **Table S3**-all stats).

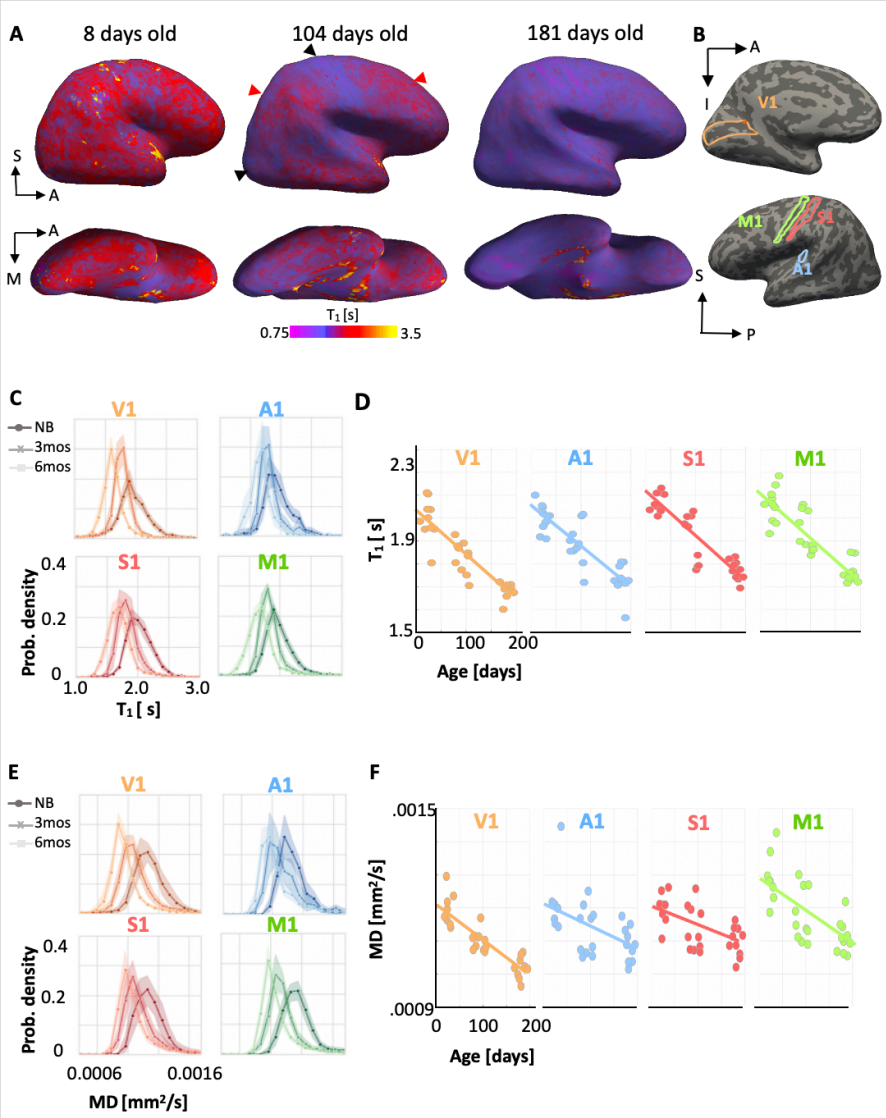

Fig 1. Primary sensory cortices are not fully developed at birth but show extensive microstructural tissue growth during the first 6 months of life. (A) Right hemisphere sagittal (top) and ventral-temporal (bottom) T_1 maps [in seconds] displayed on an inflated cortical surface of an example baby. *Left to right:* cortical T_1 at 8 days (newborn), 104 days (~ 3 months), and 181 days (~ 6 months) of age (*red/yellow:* higher T_1; *purple*: lower T_1). (B) Primary sensory-motor areas: V1, A1, M1 and S1 (*16*) on a cortical surface of this infant. (C) T_1 distributions across voxels of each area show a leftward shift from newborns (darker colors) to 6 month-olds (lighter colors). *Solid lines*: mean distribution; *shaded region*: standard error of the mean (SE) across 10 infants at each timepoint. *NB:* newborns; *3 mo:* 3 month-olds; *6 mo:* 6 month-olds. (D) T_1 linearly decreases with age in primary sensory-motor areas. *Each dot*: mean T_1 per area per infant. *Line:* Linear mixed model line fit. (E-F) Same as in C-D for MD.

As the visual system is the best understood sensory system, we used it as a model to investigate cortical microstructural development within a brain system. Visual cortex is characterized by hierarchical processing streams (*14*): the ventral stream involved in visual recognition, and the dorsal stream involved in visually guided actions and localization. In each infant and timepoint, we identified nine visual areas in the dorsal

(V1d to IPS3) and eight in the ventral (V1v to PHC2) stream by aligning the Wang atlas (*15*) (**Fig. 2A**) to each individual brain using cortex-based alignment. Then, we measured T_1 and MD in each area. Results showed that within the first 6 months of life, T_1 decreases in visual cortex on average by 0.36s – 0.54s (**Figs. 2B, 2C**). LMMs per area quantified this development, revealing that T_1 linearly decreases in all dorsal (T_1 change/slopes: -3 to -2 [ms/day], *Ps*<10^{-7}, **Fig. 2B**) and ventral visual areas (slopes: -1.9 to -1.5 [ms/day], *Ps*<10^{-6}, **Fig. 2C**, **Table S4**-all stats).

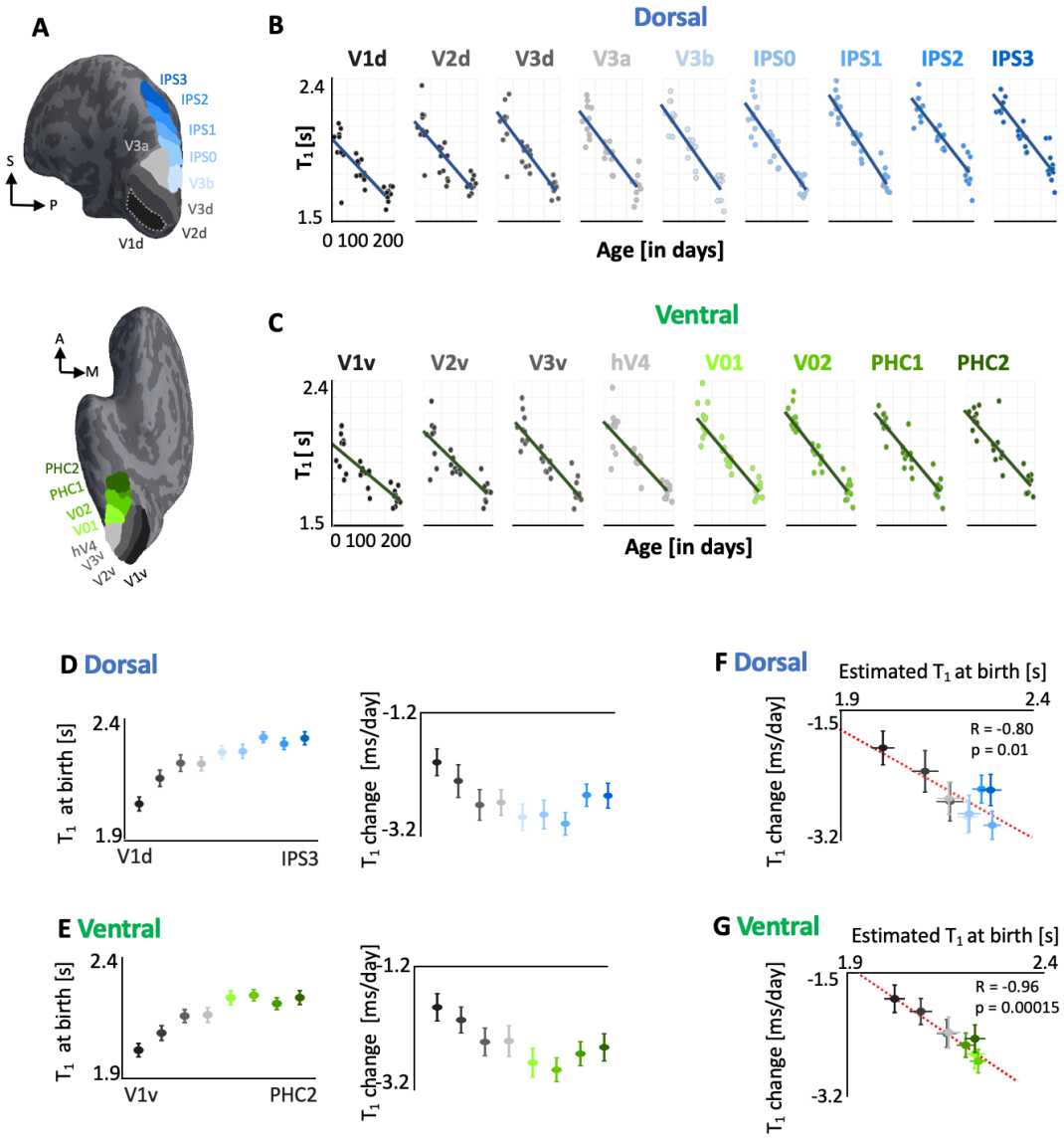

Fig 2. Hierarchical development of cortical microstructure in visual streams (A) Inflated cortical surface of an example 6-month-old infant showing nine dorsal visual (top) and eight ventral visual (bottom) areas (*15*). Areas are indicated by color. T_1 as a function of infant age in each visual area of dorsal (B) and ventral (C) streams. *Each dot:* mean T_1 per area per infant. Linear mixed model (LMM) estimates of mean T_1 (LMM intercept) and rate of T_1 development (LMM slope) in (D) dorsal and (E) ventral visual areas. Significant negative correlation between T_1 at birth and rate of T_1 development in dorsal (F) and ventral (G) streams. *Error bars:* standard error on estimates of intercepts and slopes. All data are right hemisphere; left hemisphere in **Fig. S5.**

Interestingly, examination of LMM estimates of T_1 at birth showed a systematic increase in T_1 at birth ascending the hierarchy of each processing stream. In the dorsal stream, T_1 at birth increases from V1d [2.0s±0.028s] to IPS3 [2.29s±0.027s] (**Fig. 2D**-left, **Fig. S5**); in the ventral stream, it increases from V1v [2.01s±0.026s] to PHC2 [2.21+.027s] (**Fig. 2E**-left, **Fig. S5**). However, examination of the rate of T_1 development in both streams, revealed the opposite pattern: T_1 decreased more rapidly (more negative slope) in higher-order visual areas of both dorsal (**Fig. 2D-**right) and ventral (**Fig. 2E**-right) hierarchies compared to V1. Similar results were observed with MD (**Figs. S6, S7**).

Given this systematicity, we asked: is there a link between T_1 development rate and T_1 at birth? To test this, we plotted change in T_1 (slope) vs. T_1 at birth (intercept) per area for each visual stream (**Figs. 2F,G**). Results highlighted significant negative relationships in both dorsal (left hemi: R=-0.80, P=0.01; right hemi: R=-0.80, P=0.01, **Fig. 2F**) and ventral streams (left hemi: R=-0.89, P=. 002; right hemi: R=-0.96, P=.00015, **Fig. 2G**) stream. Similar results were found in MD (**Fig. S6**).

Combined, these data reveal two intriguing features of cortical development in the infant visual system. First, ascending visual hierarchies from V1 to higher-level visual areas, cortical microstructure is gradually less mature at birth, but surprisingly develops faster. Second, the observed age-related decreases in T_1 and MD support the hypothesis of microstructural tissue growth in cortex during early infancy. A key question that remains is: what microstructural tissue compartments may underlie this systematic postnatal cortical tissue growth?

To answer this question, we leveraged the transcriptomic gene expression database of postmortem tissue samples of the Brain Span Atlas (https://www.brainspan.org) to identify candidate genes that show differential expression levels postnatally vs. prenatally. We reasoned that birth is a key developmental stage and genes expressed more postnatally than prenatally may contribute to the cortical development we observed. We examined gene expression in brain tissue samples that closely matched our *in vivo* data in anatomical location and age (postnatal samples only), including samples from primary sensory-motor areas (M1, V1, A1, V1) and higher-level visual areas (inferior parietal cortex, superior and inferior temporal cortex, **Tables S6, S7**). For each sample, we extracted RNA-Seq expression data in Reads Per Kilobase per Million (RPKM) and then determined which genes show higher postnatal vs. prenatal expression along with the fold change (FC) and statistical significance.

Result of this differential analysis generates a list of several thousand genes that are expressed significantly more in these cortical expanses postnatally than prenatally. To determine the most differentially expressed genes, we selected the genes with the largest expression changes (FC>4) and assessed their significance after Bonferroni correction ($P<5.7x10^{-6}$). **Fig. 3A** shows the expression level (per area/age) of ninety-five genes which survived these criteria and **Fig. 3B** shows their FC in descending order. Results show for the top 10 genes, for instance, expression levels increase from ~1 RPKM, prenatally, to more than ~6 RPKM, postnatally (**Fig. 3A**). Intriguingly, the top-most differentially expressed gene in primary sensory-motor and visual cortex is myelin basic protein (MBP), a gene associated with myelin generation and myelin sheath wrapping (*17*). Other myelin related genes, including myelin-associated oligodendrocytic basic protein (MOBP), myelin-associated glycoprotein (MAG), and proteolipid protein (PLP-1), are also among the top 10 most expressed postnatal genes (**Fig. 3A**).

To further elucidate the molecular and cellular pathways linked to these 95 genes, we used the ToppGene toolbox (https://toppgene.cchmc.org) (*18*). This toolbox maps a list of expressed genes to enriched physiological processes. Comparing the top 95 genes to all protein-coding genes as the background set, we found enrichment of several processes related to: (i) myelination ($P_{FDR\_corrected}=1.38x10^{-4}$), (ii) structural constituents of myelin sheath ($P_{FDR\_corrected}=2.05x10^{-5}$), (iii) axonal ensheathing ($P_{FDR\_corrected}=1.38x10^{-4}$), (iv) synaptic signaling ($P_{FDR\_corrected}=1.34x10^{-12}$), and (v) cellular components of axonal projections and dendritic spines ($P_{FDR\_corrected}=7.97x10^{-5}$) (**Fig. 3C**, **Table S8, DataSet1**). These processes remained enriched in a control analysis, in which we restricted the background gene set to genetic markers of cortical cells (neurons, astrocytes, endothelial cells, microglia, oligodendrocytes (*19*) (**DataSet2**)).

Fig 3. Transcriptomic gene analysis of cortical samples reveals that myelination and synaptic processes are cellular mechanisms of postnatal development. (A) Matrix showing gene expression levels in prenatal (19 post conceptual weeks (pcw) to 37 pcw) and postnatal (three 4-month-olds) cortical tissue samples for the 95 most differentially expressed genes. *Rows:* genes, *columns:* cortical area (acronyms in **Table S7**), *color:* expression level in reads per kilobase per million (RPKM, see colorbar). (B) Gene expression fold change (FC) between postnatal vs. prenatal cortical samples of the 95 most differentially expressed genes. (C) Gene enrichment analysis (*18*) showing the molecular and biological processes and cellular components related to these 95 genes.

In sum, our study revealed two important findings. First, decreases in cortical T_1 and MD together with gene analyses suggest that infants' cortex undergoes exuberant microstructural tissue growth related to myelination, synaptogenesis, and dendritic processes during the first 6 months of life. Consistent with *ex*

vivo data showing synaptogenesis (*3*) and dendritic growth (*20*) in primate V1 and A1 during infancy, we find no evidence for cortical tissue pruning from 0 to 6 months of age. It is possible that pruning happens later in development after this exuberant growth (*3*, *21*), or that pruning effects are smaller than microstructural growth effects, which dominate MR metrics. As gene analyses revealed that MBP is the top-most differentially expressed gene after birth, and both *ex vivo* and *in vivo* studies show that cortical T_1 decreases with higher myelin content (*10*, *13*), our data suggest that myelin contributes to T_1 decreases in cortex. These findings not only reveal that cortical myelination and synaptogenesis are dominant processes during early infancy, but also that future work should consider the impact of cortical myelination on the development of brain circuits and ultimately behavior.

Second, our results of hierarchical development of cortical T_1 and MD challenge the prevailing view that primary visual cortex is myelinated at birth (*22*, *23*) and develops faster than higher-level areas. Not only do both early and high-level visual areas continue to develop and myelinate during infancy, but high-level areas develop at faster rates. This hierarchical pattern of development overturns the prevailing theory based largely on examinations of white matter myelination at birth (*22–24*). Our results reveal that early sensory areas, like V1, do indeed have a head-start at birth, but after birth, as babies acquire sensory experiences, higher-level sensory areas develop at a rapider pace. We hypothesize that the more mature primary sensory-motor cortices at birth may provide important scaffolding for the development of cortical systems. However, the sensory richness of the postnatal environment may accelerate activity-dependent (*25*, *26*) myelination and synaptogenesis in higher-order sensory cortices.

To conclude, our longitudinal, *in vivo*, and quantitative measurements of microstructure necessitate a rethinking of how cortical microstructure emerges in babies, and open new avenues to consider the impact of cortical myelination on the development of brain function. These data have important implications for new methodologies to identify neurodevelopmental delays and disorders (*27–29*), which may lead to early inventions and better life-long outcomes.

Supplementary Materials:

Materials and Methods

Figures S1-S7

Tables S1-S8

Dataset 1: https://github.com/VPNL/babies_graymatter/genes/Dataset1

Dataset 2: https://github.com/VPNL/babies_graymatter/genes/Dataset2

References (***30–42)***

References and Notes

1. P. R. Huttenlocher, Morphometric study of human cerebral cortex development. *Neuropsychologia*. **28** (1990), doi:10.1016/0028-3932(90)90031-I.
2. R. C. Knickmeyer, S. Gouttard, C. Kang, D. Evans, K. Wilber, J. K. Smith, R. M. Hamer, W. Lin, G. Gerig, J. H. Gilmore, A structural MRI study of human brain development from birth to 2 years. *Journal of Neuroscience*. **28** (2008), doi:10.1523/JNEUROSCI.3479-08.2008.
3. P. R. Huttenlocher, A. S. Dabholkar, Regional differences in synaptogenesis in human cerebral cortex. *Journal of Comparative Neurology*. **387** (1997), doi:10.1002/(SICI)1096-9861(19971020)387:2.
4. D. J. Miller, T. Duka, C. D. Stimpson, S. J. Schapiro, W. B. Baze, M. J. McArthur, A. J. Fobbs, A. M. M. Sousa, N. Šestan, D. E. Wildman, L. Lipovich, C. W. Kuzawa, P. R. Hof, C. C. Sherwood, Prolonged myelination in human neocortical evolution. *Proceedings of the National Academy of Sciences of the United States of America*. **109** (2012), doi:10.1073/pnas.1117943109.
5. Z. Petanjek, M. Judaš, G. Šimić, M. R. Rašin, H. B. M. Uylings, P. Rakic, I. Kostović, Extraordinary neoteny of synaptic spines in the human prefrontal cortex. *Proceedings of the National Academy of Sciences of the United States of America*. **108** (2011), doi:10.1073/pnas.1105108108.
6. G. Ball, L. Srinivasan, P. Aljabar, S. J. Counsell, G. Durighel, J. v. Hajnal, M. A. Rutherford, A. D. Edwards, Development of cortical microstructure in the preterm human brain. *Proceedings of the National Academy of Sciences of the United States of America*. **110** (2013), doi:10.1073/pnas.1301652110.
7. J. Lebenberg, J. F. Mangin, B. Thirion, C. Poupon, L. Hertz-Pannier, F. Leroy, P. Adibpour, G. Dehaene-Lambertz, J. Dubois, Mapping the asynchrony of cortical maturation in the infant brain: A MRI multi-parametric clustering approach. *NeuroImage*. **185** (2019), doi:10.1016/j.neuroimage.2018.07.022.
8. S. C. L. Deoni, E. Mercure, A. Blasi, D. Gasston, A. Thomson, M. Johnson, S. C. R. Williams, D. G. M. Murphy, Mapping infant brain myelination with magnetic resonance imaging. *Journal of Neuroscience*. **31** (2011), doi:10.1523/JNEUROSCI.2106-10.2011.
9. A. Mezer, J. D. Yeatman, N. Stikov, K. N. Kay, N. J. Cho, R. F. Dougherty, M. L. Perry, J. Parvizi, L. H. Hua, K. Butts-Pauly, B. A. Wandell, Quantifying the local tissue volume and composition in individual brains with magnetic resonance imaging. *Nature Medicine*. **19** (2013), doi:10.1038/nm.3390.
10. L. J. Edwards, E. Kirilina, S. Mohammadi, N. Weiskopf, Microstructural imaging of human neocortex in vivo. *NeuroImage*. **182** (2018), , doi:10.1016/j.neuroimage.2018.02.055.
11. C. Beaulieu, The basis of anisotropic water diffusion in the nervous system - A technical review. *NMR in Biomedicine*. **15** (2002), , doi:10.1002/nbm.782.
12. J. Gomez, M. A. Barnett, V. Natu, A. Mezer, N. Palomero-Gallagher, K. S. Weiner, K. Amunts, K. Zilles, K. Grill-Spector, Microstructural proliferation in human cortex is coupled with the development of face processing. *Science*. **355** (2017), doi:10.1126/science.aag0311.
13. V. S. Natu, J. Gomez, M. Barnett, B. Jeska, E. Kirilina, C. Jaeger, Z. Zhen, S. Cox, K. S. Weiner, N. Weiskopf, K. Grill-Spector, Apparent thinning of human visual cortex during childhood is associated with myelination. *Proceedings of the National Academy of Sciences of the United States of America*. **116** (2019), doi:10.1073/pnas.1904931116.
14. L. G. Ungerleider, M. Mishkin, Two cortical visual systems. *Analysis of Visual Behavior* (1982).
15. L. Wang, R. E. B. Mruczek, M. J. Arcaro, S. Kastner, Probabilistic maps of visual topography in human cortex. *Cerebral Cortex*. **25** (2015), doi:10.1093/cercor/bhu277.
16. M. F. Glasser, T. S. Coalson, E. C. Robinson, C. D. Hacker, J. Harwell, E. Yacoub, K. Ugurbil, J. Andersson, C. F. Beckmann, M. Jenkinson, S. M. Smith, D. C. van Essen, A multi-modal parcellation of human cerebral cortex. *Nature*. **536** (2016), doi:10.1038/nature18933.
17. J. M. Boggs, Myelin basic protein: A multifunctional protein. *Cellular and Molecular Life Sciences*. **63** (2006), , doi:10.1007/s00018-006-6094-7.
18. J. Chen, E. E. Bardes, B. J. Aronow, A. G. Jegga, ToppGene Suite for gene list enrichment analysis and candidate gene prioritization. *Nucleic Acids Research*. **37** (2009), doi:10.1093/nar/gkp427.

19. A. T. McKenzie, M. Wang, M. E. Hauberg, J. F. Fullard, A. Kozlenkov, A. Keenan, Y. L. Hurd, S. Dracheva, P. Casaccia, P. Roussos, B. Zhang, Brain Cell Type Specific Gene Expression and Co-expression Network Architectures. *Scientific Reports*. **8** (2018), doi:10.1038/s41598-018-27293-5.
20. G. N. Elston, I. Fujita, Pyramidal cell development: Postnatal spinogenesis, dendritic growth, axon growth, and electrophysiology. *Frontiers in Neuroanatomy*. **8** (2014), , doi:10.3389/fnana.2014.00078.
21. J. P. Bourgeois, P. Rakic, Changes of synaptic density in the primary visual cortex of the macaque monkey from fetal to adult stage. *Journal of Neuroscience*. **13** (1993), doi:10.1523/jneurosci.13-07-02801.1993.
22. P. Flechsig, Anatomie des menschlichen Gehirns und Rückenmarks aus myelogenetischer Grundlage. . *JAMA J. Am. Med. Assoc.* . **76,** (1921).
23. P. I. Yakovlev, A.-R. Lecours, in *Regional Development of Brain in Early Life* (1967).
24. H. C. Kinney, B. A. Brody, A. S. Kloman, F. H. Gilles, Sequence of central nervous system myelination in human infancy: II. Patterns of myelination in autopsied infants. *Journal of Neuropathology and Experimental Neurology*. **47** (1988), doi:10.1097/00005072-198805000-00003.
25. R. D. Fields, Myelin - More than insulation. *Science*. **344** (2014), , doi:10.1126/science.1253851.
26. L. C. Katz, C. J. Shatz, Synaptic activity and the construction of cortical circuits. *Science*. **274** (1996), , doi:10.1126/science.274.5290.1133.
27. T. L. Jernigan, T. T. Brown, D. J. Hagler, N. Akshoomoff, H. Bartsch, E. Newman, W. K. Thompson, C. S. Bloss, S. S. Murray, N. Schork, D. N. Kennedy, J. M. Kuperman, C. McCabe, Y. Chung, O. Libiger, M. Maddox, B. J. Casey, L. Chang, T. M. Ernst, J. A. Frazier, J. R. Gruen, E. R. Sowell, T. Kenet, W. E. Kaufmann, S. Mostofsky, D. G. Amaral, A. M. Dale, The Pediatric Imaging, Neurocognition, and Genetics (PING) Data Repository. *NeuroImage*. **124** (2016), doi:10.1016/j.neuroimage.2015.04.057.
28. S. P. Fitzgibbon, S. J. Harrison, M. Jenkinson, L. Baxter, E. C. Robinson, M. Bastiani, J. Bozek, V. Karolis, L. Cordero Grande, A. N. Price, E. Hughes, A. Makropoulos, J. Passerat-Palmbach, A. Schuh, J. Gao, S. R. Farahibozorg, J. O'Muircheartaigh, J. Ciarrusta, C. O'Keeffe, J. Brandon, T. Arichi, D. Rueckert, J. v. Hajnal, A. D. Edwards, S. M. Smith, E. Duff, J. Andersson, The developing Human Connectome Project (dHCP) automated resting-state functional processing framework for newborn infants. *NeuroImage*. **223** (2020), doi:10.1016/j.neuroimage.2020.117303.
29. B. R. Howell, M. A. Styner, W. Gao, P. T. Yap, L. Wang, K. Baluyot, E. Yacoub, G. Chen, T. Potts, A. Salzwedel, G. Li, J. H. Gilmore, J. Piven, J. K. Smith, D. Shen, K. Ugurbil, H. Zhu, W. Lin, J. T. Elison, The UNC/UMN Baby Connectome Project (BCP): An overview of the study design and protocol development. *NeuroImage*. **185** (2019), , doi:10.1016/j.neuroimage.2018.03.049.
30. H. Wu, R. F. Dougherty, A. B. Kerr, K. Zhu, M. J. Middione, A. Mezer, in *21st Annu. Meet. Organ. Hum. Brain Mapp. (2015).* (2015).
31. M. Jenkinson, C. F. Beckmann, T. E. J. Behrens, M. W. Woolrich, S. M. Smith, Review FSL. *NeuroImage*. **62** (2012).
32. J. J. Moré, *The Levenberg-Marquardt algorithm: Implementation and theory* (in 105–116 (Springer, Berlin, Heidelberg, 1978)., 1978).
33. L. Zöllei, J. E. Iglesias, Y. Ou, P. E. Grant, B. Fischl, Infant FreeSurfer: An automated segmentation and surface extraction pipeline for T1-weighted neuroimaging data of infants 0–2 years. *NeuroImage*. **218** (2020), doi:10.1016/j.neuroimage.2020.116946.
34. J. D. Tournier, R. Smith, D. Raffelt, R. Tabbara, T. Dhollander, M. Pietsch, D. Christiaens, B. Jeurissen, C. H. Yeh, A. Connelly, MRtrix3: A fast, flexible and open software framework for medical image processing and visualisation. *NeuroImage*. **202** (2019), , doi:10.1016/j.neuroimage.2019.116137.
35. J. Veraart, D. S. Novikov, D. Christiaens, B. Ades-aron, J. Sijbers, E. Fieremans, Denoising of diffusion MRI using random matrix theory. *NeuroImage*. **142** (2016), doi:10.1016/j.neuroimage.2016.08.016.

36. J. L. R. Andersson, M. S. Graham, E. Zsoldos, S. N. Sotiropoulos, Incorporating outlier detection and replacement into a non-parametric framework for movement and distortion correction of diffusion MR images. *NeuroImage*. **141** (2016), doi:10.1016/j.neuroimage.2016.06.058.
37. N. J. Tustison, B. B. Avants, P. A. Cook, Y. Zheng, A. Egan, P. A. Yushkevich, J. C. Gee, N4ITK: Improved N3 bias correction. *IEEE Transactions on Medical Imaging*. **29** (2010), doi:10.1109/TMI.2010.2046908.
38. B. Fischl, M. I. Sereno, R. B. H. Tootell, A. M. Dale, High-resolution intersubject averaging and a coordinate system for the cortical surface. *Human Brain Mapping*. **8** (1999), doi:10.1002/(SICI)1097-0193(1999)8:4<272::AID-HBM10>3.0.CO;2-4.
39. J. G. Chi, E. C. Dooling, F. H. Gilles, Gyral development of the human brain. *Annals of Neurology*. **1** (1977), doi:10.1002/ana.410010109.
40. R. S. Desikan, F. Ségonne, B. Fischl, B. T. Quinn, B. C. Dickerson, D. Blacker, R. L. Buckner, A. M. Dale, R. P. Maguire, B. T. Hyman, M. S. Albert, R. J. Killiany, An automated labeling system for subdividing the human cerebral cortex on MRI scans into gyral based regions of interest. *NeuroImage*. **31** (2006), doi:10.1016/j.neuroimage.2006.01.021.
41. L. R. Dice, Measures of the Amount of Ecologic Association Between Species. *Ecology*. **26** (1945), doi:10.2307/1932409.
42. J. J. Chen, S. J. Wang, C. A. Tsai, C. J. Lin, Selection of differentially expressed genes in microarray data analysis. *Pharmacogenomics Journal*. **7** (2007), doi:10.1038/sj.tpj.6500412.

Acknowledgements: We would like to acknowledge Amy Kang, KK Barrows, Javier Marquis Lopez, Laura Villalobos, Lois Williams, and Alex Rezai for their contributions with gray and white matter segmentations of the infant brains and Caitlyn Estrada for her contribution to data collection. We would also like to thank Jiyeong Ha for her contributions towards the quality assurance check on the delineations of brain regions on the infant and adult brains. Additionally, we would like to thank Fiorella Carla Grandi for feedback and advice on the gene analyses.

Funding: Wu Tsai Neurosciences Institute Big Ideas Grant Phase 1, NIH 1 R21 EY030588

Author contributions: MR: study design, data acquisition, data preprocessing, statistical analysis, manuscript writing; VSN: data preprocessing, statistical analysis, manuscript writing; HW: sequence development; FRQ: participant recruitment, data acquisition, data preprocessing; HK: participant recruitment, data acquisition, data preprocessing;; NLA: data collection; MG: data preprocessing (dMRI), SB: data preprocessing (artificial T1-weighted image), AAM: sequence development, KGS: designed the study, oversaw all components of the study, and wrote the manuscript. All co-authors read and approved the submitted manuscript.

Competing interests: Authors declare no competing interests.

Data and materials availability: Data, code, and materials used in the analysis will be made available with publication on GitHub (https://github.com/VPNL/babies_graymatter).

Materials and Methods

Participants. 16 full-term and healthy infants (7 female) were recruited to participate in this study. 3 infants provided no usable data because they could not stay asleep once the MRI sequences started. Here, we report data from 13 infants (6 female) across three age timepoints: newborn/0 months [8-37 days], 3 months [78-106 days], and 6 months [167-195 days], with 10 participants per timepoint. Two participants were reinvited to complete scans for their 6-months session that could not be completed during the first try. Both

rescans were performed within 7 days and participants were still within age range for the 6-month timepoint. The participant population was racially and ethnically diverse reflecting the population of the San Francisco Bay Area, including two Hispanic, nine Caucasian, two Asian, three multiracial (2 Asian and Caucasian; 1 Native Hawaiian or Other Pacific Islander) participants. Seven out of these 13 infants participated in MRI in all three timepoints (0, 3, 6 months). Due to the Covid-19 pandemic and restricted research guidelines, data acquisition was halted. Consequently, the remaining infants participated in either 1 or 2 sessions. Participation of the 13 infants whose data is reported in this study is summarized in **Table S1**.

Expectant mother and infant screening procedure

Expectant mothers and their infants in our study were recruited from the San Francisco Bay Area using social media platforms. We performed a two-step screening process for expectant mothers. First, mothers were screened over the phone for eligibility based on exclusionary criteria designed to recruit a sample of typically developing infants and second, eligible expectant mothers were screened once again after giving birth. Exclusionary criteria for expectant mothers were as follows: recreational drug use during pregnancy, significant alcohol use during pregnancy (more than 3 instances of alcohol consumption per trimester; more than 1 drink per occasion), lifetime diagnosis of autism spectrum disorder or a disorder involving psychosis or mania, taking prescription medications for any of these disorders during pregnancy, insufficient written or spoken English ability to comprehend study instructions, and learning disabilities. Exclusionary criteria for infants were preterm birth (<37 gestational weeks), low birthweight (<5 lbs. 8 oz), small height (<18 inches), any congenital, genetic, or neurological disorders, visual problems, complications during birth that involved the infant (e.g., NICU stay), history of head trauma, and contraindications for MRI (e.g., metal implants).

MRI (magnetic resonance imaging) Procedure.

We acquired T2-weighted MRI, quantitative MRI (qMRI), and diffusion MRI (qMRI) data for each infant and time point. Study protocols for these scans were approved by the Stanford University Internal Review Board on Human Subjects Research. Scanning sessions were scheduled in the evenings close in time to the infants' typical bedtime. The duration of each session lasted between 2.5 – 5 hours including time to prepare the infant and waiting time for them to fall asleep. Upon arrival, caregivers provided written, informed consent for themselves and their infant to participate in the study. Before entering the MRI suite, both caregiver and infant were checked to ensure that they were safe and metal-free to enter the MRI suite. Before entering the MRI suite, caregivers changed the infants into MR safe cotton onesies and footed pants provided by the researchers. The infant was swaddled with a blanket with their hands to their sides to avoid their hands creating a loop during MRI. During scans of newborn infants, an MR safe plastic immobilizer (MedVac, www.supertechx-ray.com) was used to stabilize the infant and their head position. Once the infant was ready for scanning, the caregiver and infant entered the MR suite. The caregiver was instructed to follow their child's typical sleep routine. As the infant was falling asleep, researchers inserted soft wax earplugs into the infant's ears. Once the infant was asleep, the caregiver was instructed to gently place the infant on a makeshift cradle on the scanner bed, created by placing weighted bags at the edges of the bed to prevent any side-to-side movement. Finally, to lower sound transmission, MRI compatible neonatal Noise Attenuators (https://newborncare.natus.com/products-services/newborn-care-products/nursery-essentials/minimuffs-neonatal-noise-attenuators) were placed on the infant's ears and additional pads were also placed around the infant's head to stabilize head motion. An experimenter stayed inside the MR suite with the infant during the entire scan in case the infant woke up during scanning. For additional monitoring of the infant's safety and motion quality an infrared camera was affixed to the head coil and positioned for viewing the infant's face in the scanner. The researcher operating the scanner monitored the infant via the camera feed, which allowed for the scan to be stopped immediately if the infant showed signs of waking or

distress. This setup allowed tracking the infant's motion; scans were stopped and repeated if there was excessive head motion.

Data Quality Assurance during MRI

To ensure high data quality, in addition to real-time monitoring of the infant's motion via an infrared camera, acquired scans were assessed immediately after acquisition of each sequence and repeated if necessary. Factors for repetition included head motion detected on the infrared camera, or head motion detected on the acquired MR images reflected in blurring of otherwise detailed anatomical images and partial voluming effects. On average, 50% of all scans across infants were successful on the first try while the rest had to be repeated.

Data Acquisition

All participants participated in multiple scans in each session to obtain anatomical MRI, quantitative MRI (qMRI), and diffusion MRI (dMRI) data. Data were acquired at two identical 3T GE Discovery MR750 Scanners (GE Healthcare) and Nova 32-ch head coils (Nova Medical) located at Stanford University: (i) Center for Cognitive and Neurobiological Imaging (CNI) and (ii) Lucas Imaging Center. As infants have low weight, all imaging was done with Normal SAR level to ensure their safety.

Anatomical MRI

T2-weighted: T2-weighted images were acquired for participants in each of 0, 3, 6 months timepoints. T2-weighed image acquisition parameters: TE=124 ms; TR = 3650ms; echo train length = 120; voxel size = 0.8mm^3; FOV=20.5cm; Scan time: 4 min and 5 sec.

Quantitative MRI

Spoiled-gradient echo images (SPGR): were acquired for all participants in each of 0, 3, 6 months. These images were used together with the IR-EPI sequence to generate whole-brain synthetic T1-weighted images. We acquired 4 SPGRs whole brain images with different flip angles: $\alpha = 4°, 10°, 15°, 20°$; TE=3ms; TR =14ms; voxel size=1mm^3; number of slices=120; FOV=22.4cm; Scan time: (4:55 min) x 4.

Inversion-recovery EPI (IR-EPI)

IR-EPI images were acquired from all participants in each of 0, 3, 6 months timepoints. We acquired multiple inversion times (TI) in the IR-EPI using a slice-shuffling technique (*30*): 20 TIs with the first TI=50ms and TI interval=150ms; we also acquired a second IR-EPI with reverse phase encoding direction. Other acquisition parameters are voxel size = 2mm^3; number of slices=60; FOV=20cm; in-plane/through-plane acceleration = 1/3; Scan time=1:45 min) x 2.

Diffusion MRI

We obtained dMRI data from 9 newborn participants, and 10 participants at 3 months and 6 months of age. One newborn woke up prior to run completion and we could not complete dMRI acquisition. dMRI parameters: multi-shell, #diffusion directions/b-value = 9/0, 30/700, 64/2000; TE = 75.7 ms; TR=2800ms; voxel size = 2mm^3; number of slices=60; FOV=20cm; in-plane/through-plane acceleration = 1/3; Scan time: 5:08 min. We also acquired a short dMRI scan with reverse phase encoding direction and only 6 b=0 images (scan time 0:20 min).

Data Analysis

The data analysis pipeline is summarized in **Fig. S1**. In brief, IR-EPI data were used to estimate T_1 relaxation time at each voxel. These data were also used together with the SPGRs to generate synthetic

T1-weighted whole brain anatomies of each infant at each timepoint. All data from that timepoint were aligned to this anatomical image. T2-weighted images were used for segmentation of gray-white matter to generate cortical surface reconstructions and dMRI data were used to estimate MD in each voxel. All infant data were kept in native space as all analyses were performed within-subject and within-timepoint.

Quantitative T_1 relaxation time modeling

The signal equation of T_1 relaxation of an inversion-recovery sequence is an exponential decay:

$$\boldsymbol{S(t) = a(1 - be^{-t/T1})}$$

where t is the inversion time, a is proportional to the initial magnetization of the voxel, b is the effective inversion coefficient of the voxel (for perfect inversion $b=2$). To work with magnitude images, we took the absolute value of the above signal equation and used it as the fitting model.

First, as part of the preprocessing, we performed susceptibility-induced distortion correction on the IR-EPI images using FSL's (*31*) top-up correction and the IR-EPI acquisition with reverse phase encoding direction. We then used the distortion corrected images to fit the above T_1 relaxation signal model using a multi-dimensional Levenberg-Marquardt algorithm (*32*). The output of the algorithm is the estimated T_1 in each voxel as well as the model goodness of fit (R^2) value in each voxel.

Generation of T1-weighted whole brain anatomies

From the SPGRs and IR-EPI scans, synthetic T1-weighted whole brain images were generated using mrQ software (https://github.com/mezera/mrQ). We analyzed all data in the native infant space and did not align to any template brain. All data (T2-weighted-anatomy, quantitative T_1 relaxation estimates, and MRI data) from a given timepoint were aligned to this brain volume (**Fig. S1**).

Generation of cortical surfaces

To generate cortical surface reconstructions, we used both T2-weighted and synthetic T1-weighted anatomies. We used multiple steps to generate accurate cortical surface reconstructions of each infant's brain at each timepoint. (1) An initial segmentation of gray and white matter was generated from the synthetic T1-weighted brain volume using infant FreeSurfer's automatic segmentation code developed for infant data (infant-recon-all; https://surfer.nmr.mgh.harvard.edu/fswiki/infantFS) (*33*). This initial segmentation generates pial and white matter surfaces, and surfaces of curvature, thickness, surface area. However, this initial FreeSurfer's segmentation misses significant portions of the infant's gray matter, as the contrast of infants' T1-weighted images were not differentiated enough between gray and white matter to generate an accurate segmentation. (2) We used T2-weighted anatomical images, which have a better contrast between gray and white matter in infants, and an independent brain extraction toolbox (Brain Extraction and Analysis Toolbox, iBEAT, v:2.0 cloud processing, https://ibeat.wildapricot.org/) to generate more accurate white and gray matter segmentations. (3) The iBEAT segmentation was further manually corrected to fix segmentation any additional errors (such as holes and handles) using ITK-SNAP (http://www.itksnap.org/) in white matter as well as gray matter. (4) The manually corrected iBEAT segmentation was aligned to the T1-weighted anatomy that was used for the FreeSurfer segmentation using manual rigid body alignment in ITK-SNAP (**Fig. S1**). (5) This aligned and segmented volume was then reinstalled into FreeSurfer using software we developed based on infant FreeSurfer functions (https://github.com/VPNL/babies_graymatter). This process updates the white matter segmentation and the cortical surfaces in the subject's FreeSurfer directory to render the accurate surfaces (**Fig. S1**). This accurate surface was used for visualization, and cortex-based registration with atlases.

dMRI

DMRI data were preprocessed using a combination of tools from mrTrix3 (https://github.com/MRtrix3/mrtrix3) (*34*) and mrDiffusion toolbox (http://github.com/vistalab/vistasoft). (1) We denoised the data using a principal component analysis (*35*) (2) We used FSL's top-up tool (https://fsl.fmrib.ox.ac.uk/) and one image collected in the opposite phase-encoding direction to correct for susceptibility-induced distortions. (3) We used FSL's eddy to perform eddy current and motion corrections. Motion correction included outlier slice detection and replacement (*36*) (4) We performed bias correction using ANTs (*37*) (5) These preprocessed dMRI images were registered to the whole-brain T2-weighted anatomy using whole-brain rigid-body registration in a two-stage model with a coarse-to-fine approach that maximized mutual information. (6) mrTrix3 software was used to fit tensors to each voxel using a least-squares algorithm that removes outliers. From the kurtosis tensor files, we estimated mean diffusivity (MD) maps in each voxel of the brain.

dMRI quality assurance

Out of the 29 dMRI acquisitions, one newborn acquisition was missing the reverse phase encoding image required for susceptibility correction. Thus, we report data from eight newborns, ten 3-month-olds and ten 6-month-olds. Across all acquisitions, less than 5.0% ± 0.7% of dMRI images were identified as outliers by FSL's eddy tool. We found no significant effect of age across the outliers (no main effect of age: $F_{2,25}$=2.84, *P*=0.08, newborn:1.20±0.83; 3 months:0.4±0.40; 6 months: 0.67±0.85) suggesting that the developmental data was well controlled across all ages of infants.

Delineation of the primary sensory cortices and ventral and dorsal visual areas

Our goal was to examine developmental changes in quantitative T_1 and MD in the gray matter of four primary sensory-motor cortices as well as across the ventral and dorsal visual processing streams from 0 to 6 months of age. In order to delineate these regions in infants, we used brain atlases that delineate these regions. Each atlas is available on the FreeSurfer adult average brain and was projected to each individual participant's cortical surface at each timepoint using infant FreeSurfer's cortical-based alignment tool. Without functional data, cortex-based alignment is the most accurate method for defining brain areas in individual brains from atlases (*38*). Critically, the major sulci and gyri that are used for cortex-based alignment are present at birth (*39*) and are visible on the cortical surface reconstructions of each of our infants. We used the Glasser atlas (*16*) to delineate the primary visual (V1), primary auditory (A1), primary motor (M1), and primary somatosensory (S1) cortices. We used the Wang atlas(*15*) to delineate 9 regions spanning the dorsal visual stream (V1d, V2d, V3d, V3a, V3b, IPS0, IPS1, IPS2, and IPS3) and 8 regions spanning the ventral visual stream (V1v, V2v, V3v, hV4, V01, V02, PHC1, and PHC2) in each participant's brain.

Quality check on the delineation of regions of interest (ROIs).

As we used cortex-based alignment and atlases developed for the adult brain to define areas in the infant brain, we sought to test how well the ROIs identified in infants' brains compared to those identified in adults' brains. We reasoned that if regions identified from adult atlases would show better correspondence to manually defined regions in adults than infants, it would indicate that these atlases are in optimal for infants. To test this, we compared how the calcarine sulcus manually defined on each individual brain compares to the cortex based aligned calcarine sulcus from the Desikan atlas (an anatomical parcellation of the brain, in the average adult FreeSurfer cortical surface (*40*). The manually defined calcarine sulcus was defined from the posterior end of the occipital pole to the prostriate (ProS) - a region along the anterior bank of the

parietal-occipital sulcus. We chose the calcarine sulcus as the benchmark because V1 is located in the calcarine sulcus and it can be identified anatomically in each individual brain. In each infant and timepoint (*N*=30) and 10 adults (ages 22-27; from our previous study (*13*)), we calculated the overlap between the Desikan-calcarine and individual-subject-calcarine using the dice coefficient (*41*). We found that the dice coefficient was 0.66±0.10 (Mean±SD) in infants and 0.67±.05 in adults. There were no significant age-related differences in dice-coefficients between infants and adults (no significant main effect of age: $F_{1,76}$ =.02, *P*=.89, 2-way analysis of variance (ANOVA) with factors of age group (infant/adult) and hemisphere (left/right) and no significant differences between hemispheres ($F_{1,76}$ =.02, *P*=.88). This analysis suggests that cortex-based alignment of brain atlases based on adult templates to infants' cortical surfaces is similar in quality to this transformation in adults.

Analysis of mean T_1 and MD in cortical areas and their development

After delineating brain areas in each participant, we calculated the distribution and mean T_1 relaxation time and mean diffusivity (MD) in each participant and timepoint. We used linear mixed models (LMMs) to determine if there were age-related changes of T_1 and MD within and across areas. LMMs were fit using the MATLAB 2017b function *fitlme*. In order to quantify the development of T_1 and MD, for each area we fit a LMM relating the mean T_1 (or MD) of that area to participants' age [in days]. We ran two types of LMM per area and data type: (1) LMM with random intercept/fixed slope model, which allows only the intercepts to vary across participants and accounts for the fact that the same infants participated across multiple timepoints, and (2) LMM with random intercept/random slope model, which allows both intercepts and slopes to vary across participants. Results revealed that the random intercept/fixed slope model fitted the data best in all cases (in all model comparisons: Ps<0.05). Thus, we report the parameters of the LMMs with random intercepts in all our analyses below:

$$mean\ T_1\ (or\ mean\ MD) \sim age\ of\ infant\ in\ days + (1|infant)$$

where *Mean T_1 (MD)* is the dependent variable, age is a continuous predictor (fixed effect), and the term: 1 | infant indicates that random intercepts are used for each participant. Per model we obtained: (1) the intercept, which represented the values of *T_1 (MD)* at birth, and (2) the average slope, which represented the rate of *T_1 (MD*) development. The linear fits of the LMMs are plotted in **Figs. 1-2** and **Figs. S3-S6** and we report slopes, and significant levels (Ps) of all areas in both hemispheres in **Tables S2-S5** below. Since we ran LMMs for each area individually, we performed Bonferroni correction for multiple comparisons for each analysis: (1) across primary sensory-motor cortices (4 areas, 6 comparisons), (2) across the dorsal visual stream (9 areas, 36 comparisons), and (3) across the ventral visual stream (8 areas, 28 comparisons).

Transcriptomic gene data analysis of postnatal versus prenatal tissue samples

In order to assess what microstructural tissue compartments may be linked to the observed postnatal tissue growth in cortex related to decrease in T_1 and MD, we used the transcriptomic gene expression database of post-mortem tissue samples made available by the Brain Span Atlas (https://www.brainspan.org). We examined: (1) if there were differences in the expression levels for genes in the postnatal tissue samples as compared to the prenatal tissue samples and (2) if so, what cellular and biological processes are related to these genes of interest. In order to closely match our *in vivo* data, we selected the postmortem postnatal tissue samples within our *in vivo* age range (0 to 6 months). Prenatal samples were between 19 post conceptual weeks (pcw) to 37 pcw, which is just prior to birth. **Table S6** includes demographic details of the postnatal and prenatal samples. Within these postmortem samples, we compared tissue from primary sensory cortices (V1, M1, S1, and A1) and parietal and temporal regions overlapping visual regions of the

dorsal and ventral visual streams, respectively, to match our *in vivo* data (**Table S7** for the complete list of brain regions from individual prenatal and postnatal samples).

The differential analysis provides information about which genes are differentially expressed when we compared our target (postnatal) versus control (prenatal) sample sets. Specifically, differential expression-level analysis reveals a list of several thousand genes along with the gene level RNA-Sequencing expression data in reads per kilobase per million (RPKM, data were log2-scaled). The analysis also estimated how many more times the genes were expressed postnatally vs prenatally (fold changes, FC) and provides the statistical significance of the contrast (*p*-values). Fold change is measured as the average log2(intensity/expression) values of all samples in the target sample minus the average log2(intensity/expression) of the control samples. As standard practice (*42*) we applied two thresholds: (1) a threshold of fold change: FC>4) and (2) a Bonferroni correction ($P<5.7x10^{-6}$) related to the differential analysis. Ninety-five genes passed these thresholds.

Functional enrichment

Next, to assess what molecular and biological processes are linked to our top gene list we inputted the list of genes to a toolbox created for gene list enrichment analysis (ToppGene https://toppgene.cchmc.org) (*18*) Specifically, this toolbox identifies the biological pathways that are enriched (over-represented) by the expression of the genes of interest more than that would be expected by chance. Each gene is compared with the genes related to a specific pathway and a p-value of the enrichment of a pathway is computed and multiple-test correction is applied. A table of biological, molecular, and cellular processes related to this list of genes is derived from this analysis. A Benjamini–Hochberg False Discovery Rate (FDR) was applied as a multiple comparisons adjustment. Information on the biological pathways related to the top-most genes, is ranked by statistical significance of functional enrichment ($-\log_{10}$ (p-value FDR). We performed this analysis first using (i) all protein-coding genes in the ToppGene database as the background reference set and (ii) only including genetic markers of cortical cells as the background reference set (N_{genes}=5000) including neurons, astrocytes, endothelial cells, microglia, oligodendrocytes (*19*) see **Table S8** for the FDR corrected p-values of the molecular functions, biological processes, and cellular processes listed in **Fig. 3c**. Complete gene ontology lists without and with background gene sets can be found on GitHub: https://github.com/VPNL/babies_graymatter/genes/Dataset1
and https://github.com/VPNL/babies_graymatter/genes/Dataset2

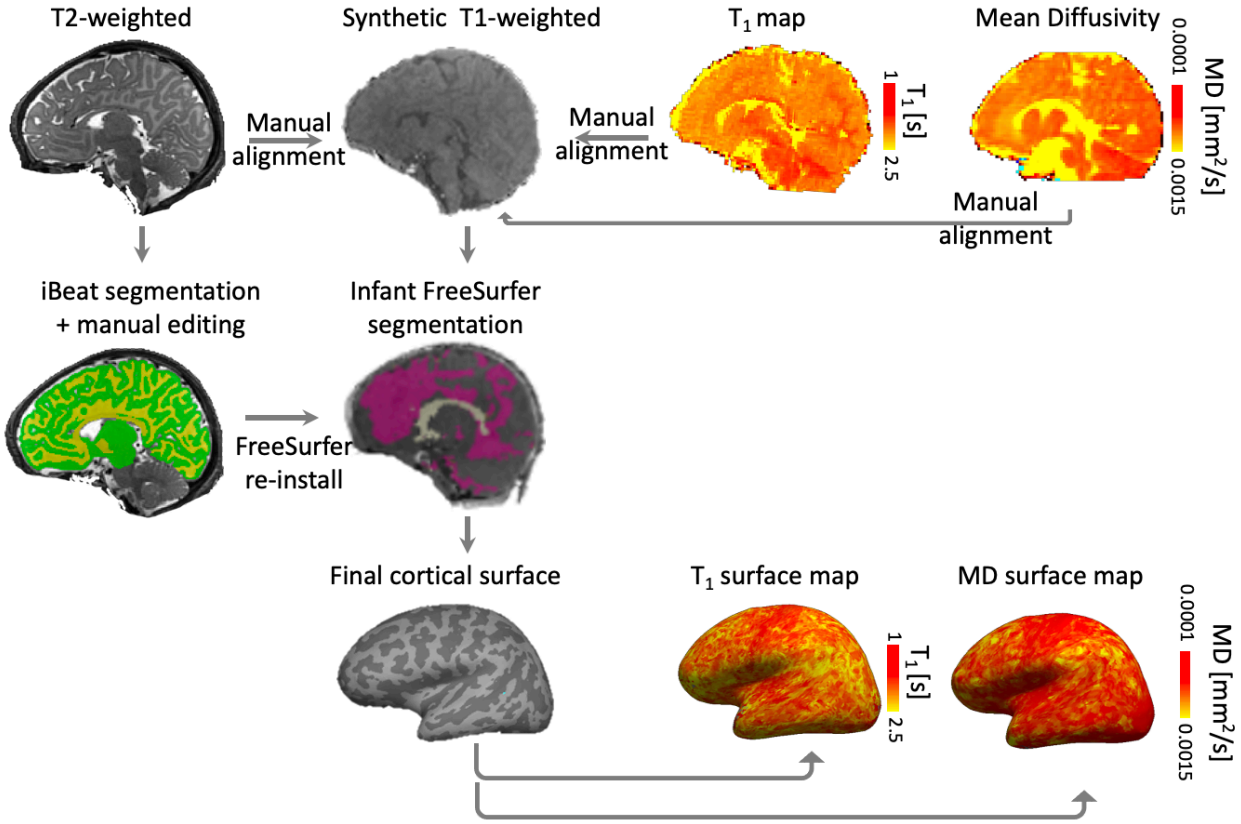

Supplementary Figure 1. MRI data preprocessing pipeline. Schematic showing the preprocessing pipeline associated with obtaining the white and gray matter segmentations for generating the cortical surfaces and quantitative T_1 and mean diffusivity (MD) maps per individual baby brain.

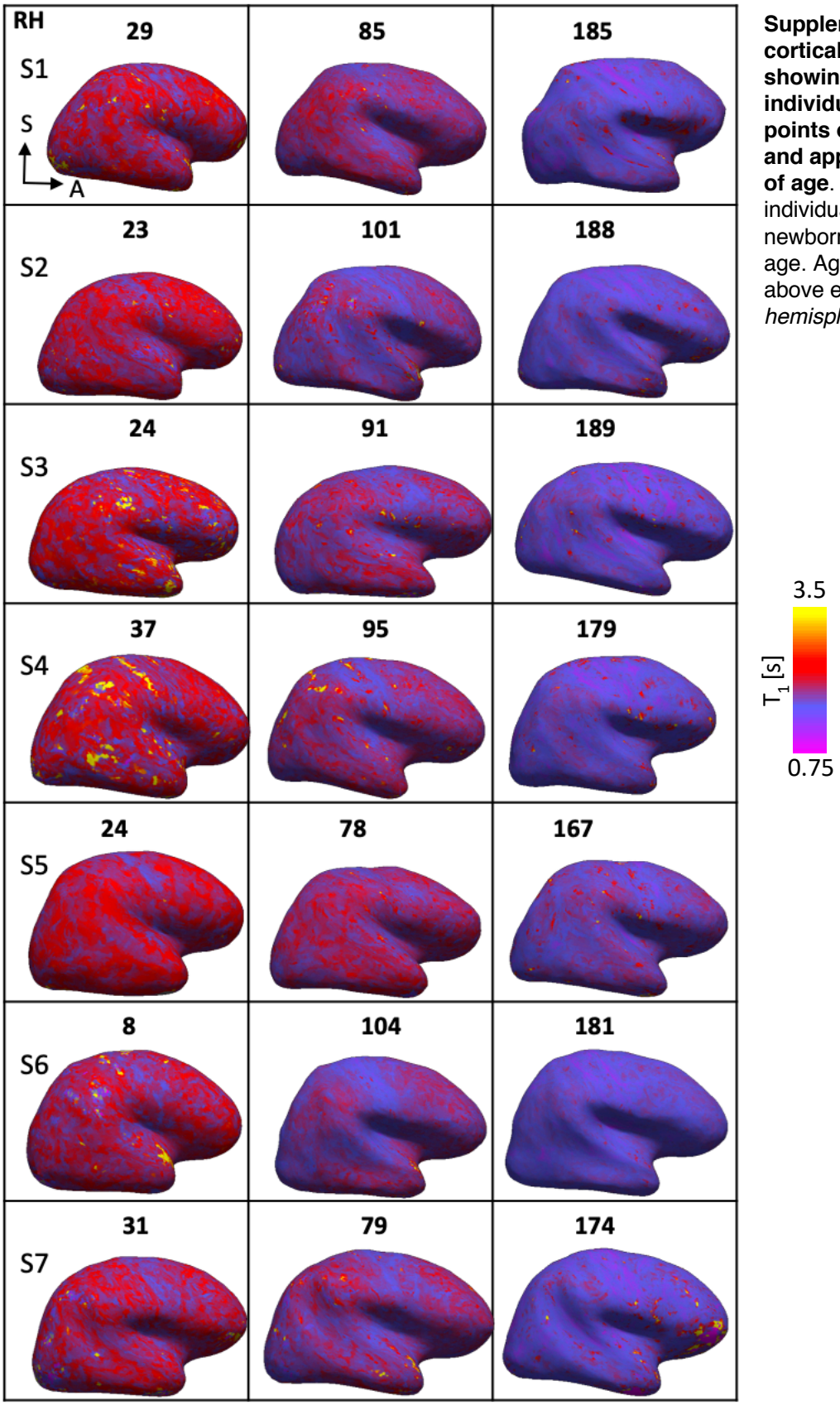

Supplementary Figure 2. Right cortical surfaces in the lateral view showing T_1 development in seven individual babies across three time points of development: newborns, and approximately 3 and 6 months of age. Each row represents an individual baby. T_1 [s] decreases from newborn (red) to 6 months (purple) of age. Age at scan (in days) isindicated above each cortical surface. *RH: right hemisphere, S: superior, A: anterior.*

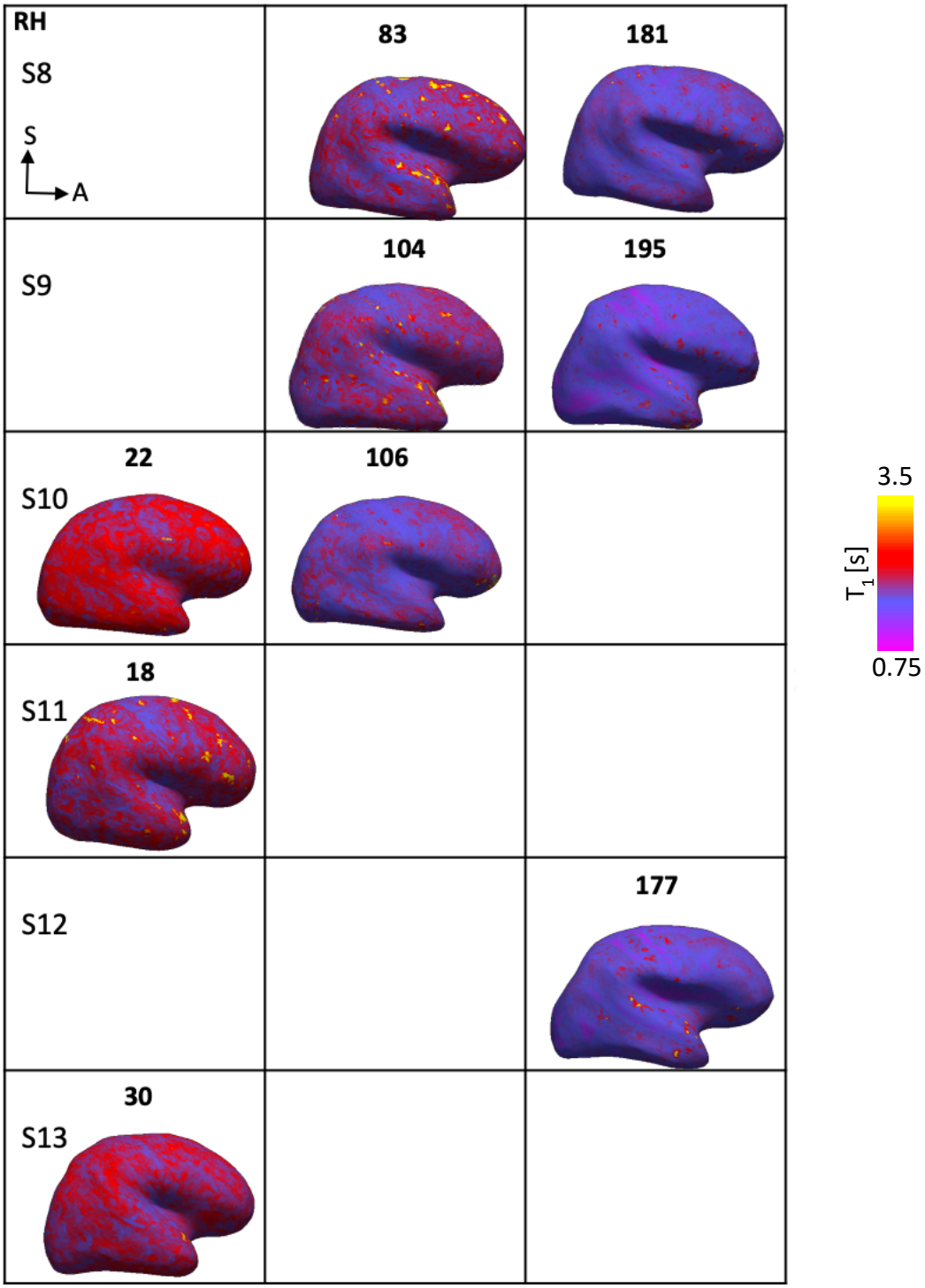

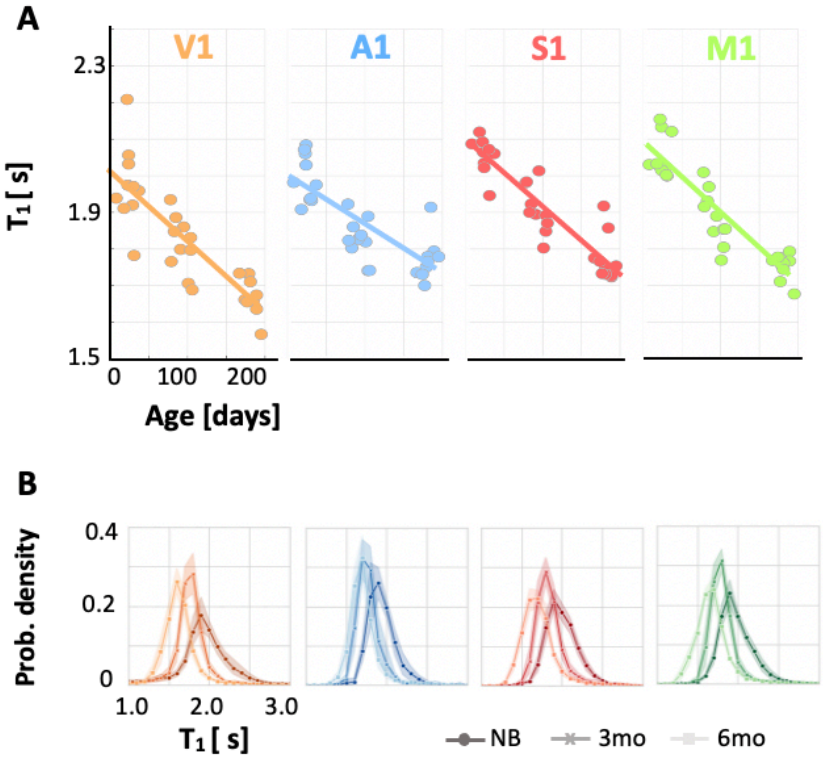

Supplementary Figure 3. Mean T_1 in four early sensory regions in the left hemisphere decreases with age in the first six months of infant life. (A) Significant decrease in T_1 with age in the four primary sensory-motor cortices (*V1: primary visual cortex, A1: primary auditory cortex, S1: primary somatosensory cortex, M1: primary motor cortex*); slopes and significance (p-values) in **Table S2**. Each dot represents mean T_1 of an infant's region of interest. (B) Distribution of T_1 across voxels in each area decreases from newborns (darker colors) to 6-month-olds (lighter colors). *Solid lines:* mean distribution across participants; *shaded region:* standard error of the mean (SE) across 10 infants in each timepoint. *NB:* newborns; *3 mo:* 3 month-olds; *6 mo:* 6 month-olds.

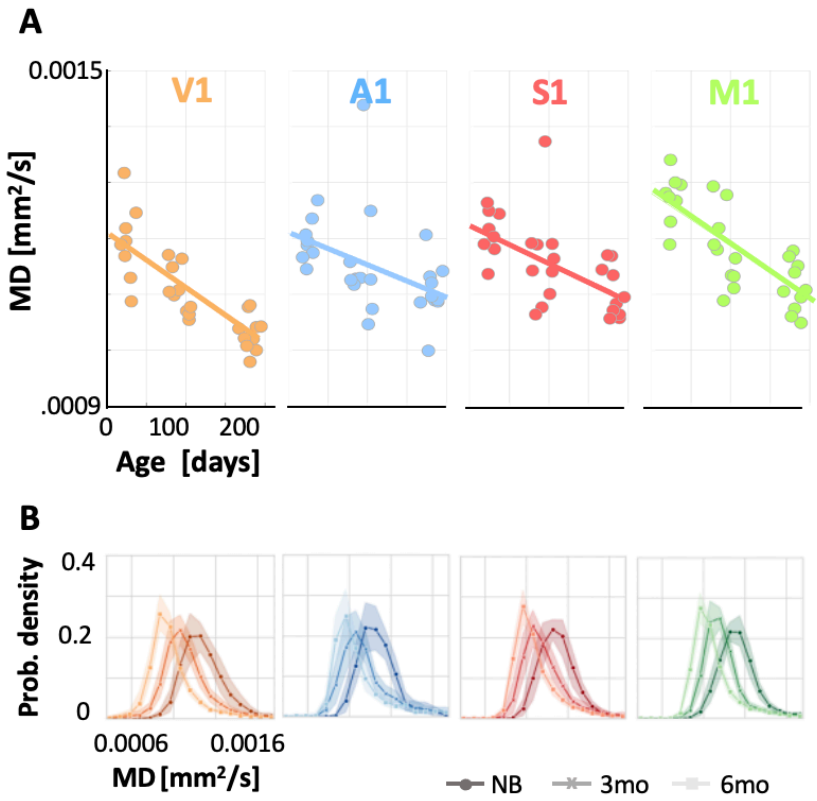

Supplementary Figure 4. Mean MD in four early sensory regions in the left hemispheres decreases with age in the first six months of infant life. (A) Significant decrease in MD with age in the four primary sensory-motor cortices (*V1: primary visual area, A1: primary auditory area, S1: primary somatosensory area, M1: primary motor area).* Slopes and p-values in **Table S3**. Each dot represents the mean MD of an infant's region of interest. (B) Distribution of MD across voxels of the four primary sensory-motor cortices shows broader distribution of MD at birth as compared to that at six months (darker colored lines: newborns). In all primary sensory-motor regions the mean MD significantly decreases from 0.0012mm²/s ±6.8x10-5 (M±SD) at 0 month to 0.0011 mm²/s ± 7.59x10-5 at 3 months to 0.0011 ± 5.52x10-5 at 6 months. Solid lines indicate mean, shaded region indicates standard error across 10 participants at each timepoint *NB:* newborns; *3 mo:* 3 month-olds; *6 mo:* 6 month-olds.

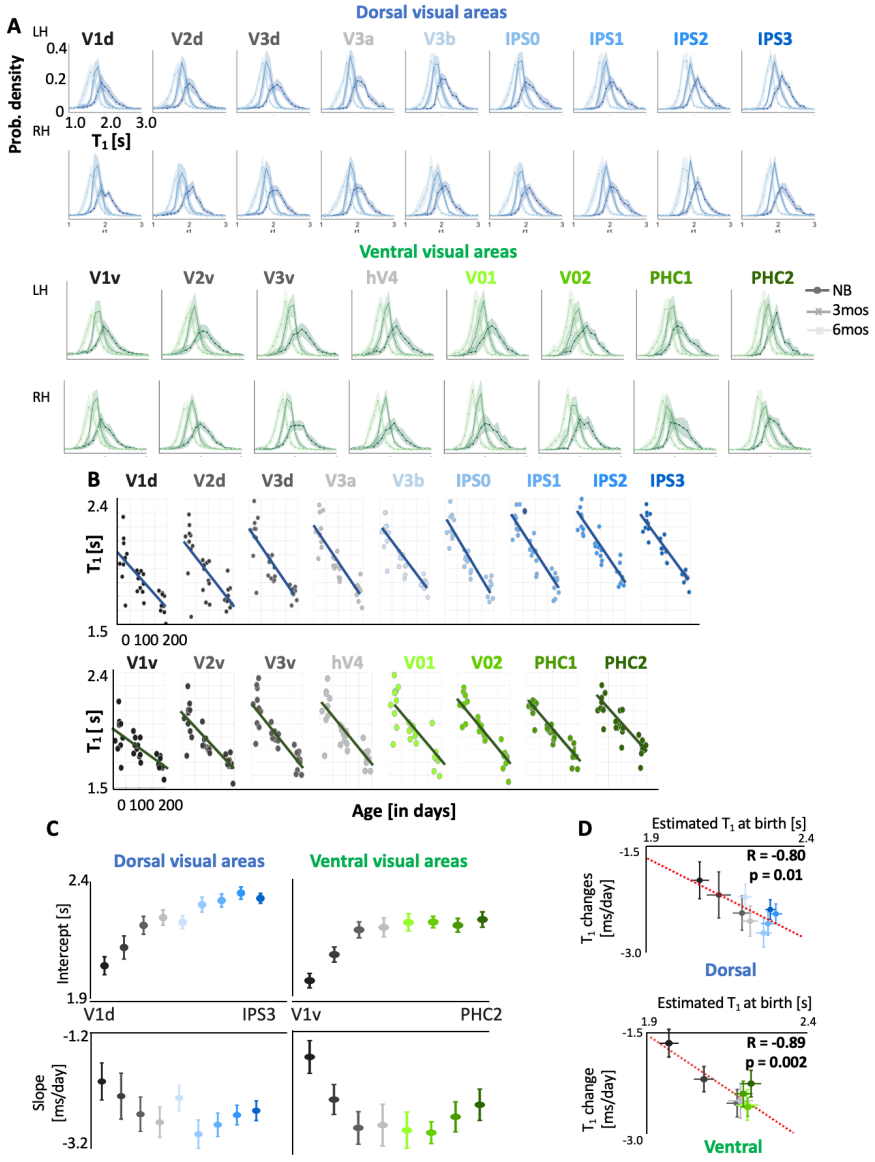

Supplementary Figure 5. Hierarchical T_1 development in the left dorsal and ventral visual streams during early infancy. (A) Distributions of T_1 in dorsal and ventral visual regions in the left and right hemispheres. Distributions shift leftward with age in the first six months of infant life. *LH/RH:* left/right hemisphere. (B) Developmental trajectory of T_1 in the first 6 months of life. *Top:* in left dorsal stream (V1d to IPS3). *Bottom:* left ventral stream (V1v to PHC2). T_1 linearly decreases in all ventral and dorsal visual areas. Each dot represents mean T_1 per ROI per infant. (C) *Top*: Mean T_1 at birth in the left dorsal and ventral streams (measured as intercepts of linear mixed model per region) shows a hierarchical development with lower T_1 in posterior than dorsal/anterior regions of the stream. *Bottom:* Developmental rate of T_1 in dorsal and ventral visual regions (measured as slopes of linear models). Interestingly, comparison of LMM estimates of T_1 at birth (intercept) across visual areas shows a gradual increase of cortical T_1 at birth across the visual hierarchy, in both the dorsal stream, from V1d [2.01s$\pm$0.036] to IPS3 [2.28s$\pm$0.019] and the ventral stream, from V1v [1.96s$\pm$0.03] to PHC2 [2.22s+0.03], suggest that cortical microstructure is gradually more mature when traversing down the hierarchy to earlier cortices with V1 being denser at birth. (D) Significant negative correlation between T_1 at birth and rate of T_1 development in left dorsal and ventral visual streams. *Error bars:* standard error on estimates of intercepts and slopes.

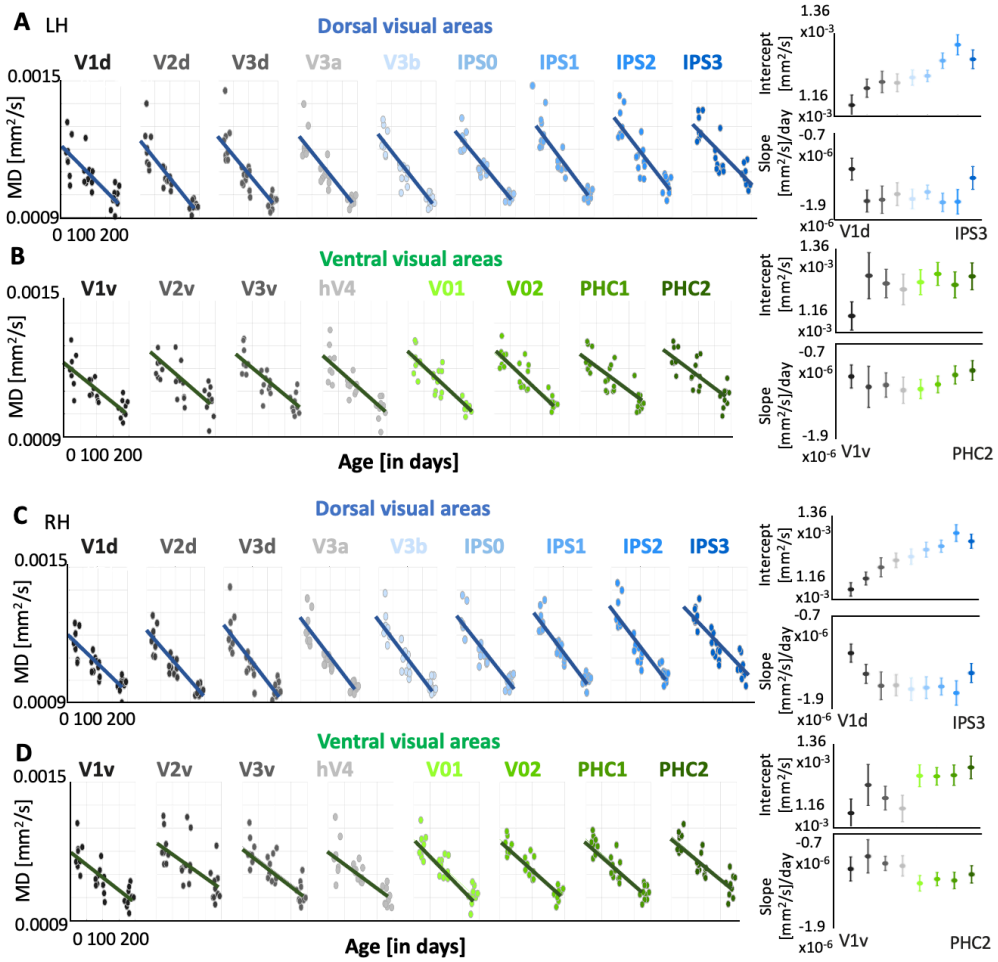

Supplementary Figure 6. Hierarchical MD development in the dorsal and ventral visual streams in the left and right hemisphere during early infancy. (A-C). Left to right shows the developmental trajectory of MD in the first 6 months of life, in the left and right dorsal visual streams (V1d to IPS3) respectively. MD linearly decreases in all dorsal visual areas; slopes and p-values in **Table S5**. Each dot represents mean MD per ROI per infant. The slopes and intercepts of each LMM are shown on the right-side of each panel. Mean MD at birth in dorsal (measured as intercepts of linear mixed model per region) shows a hierarchical development with lower MD in posterior than dorsal/anterior regions of the stream. (B-D) same as in A-C but in the ventral stream (V1v to PHC2). Interestingly, comparison of LMM estimates of MD at birth (intercept) across visual areas shows a gradual increase of cortical MD at birth across the visual hierarchy, in both the dorsal visual stream, from V1d [left: 0.0012mm²/s±2.21e-5; right 0.0012mm²/s±1.63e-5] to IPS3 [left: 0.0013mm²/s±2.205e-5; right: 0.0013mm²/s±1.70e-5] and the ventral visual stream, from V1v [left: 0.0012mm²/s ±1.83e-5; right:0.0012mm²/s±1.97e-5] to PHC2 [left: 0.013mm²/s +1.74e-5; right: 0.0013mm²/s ±1.58e-5]. These data suggest that cortical microstructure is gradually less mature when traversing the visual hierarchies from V1 to high-level visual areas. There is also a significant negative relationship between MD slopes and intercepts in the right dorsal stream (R=-0.70, P=.03), trends in the right ventral (R=-0.56, P=0.15) and left dorsal streams (R=-0.41, P=0.2), and is not significant in left ventral stream (R=-0.18, P=0.65). This relationship is less strong with MD estimates than those for T_1. *LH/RH: left/right hemisphere.*

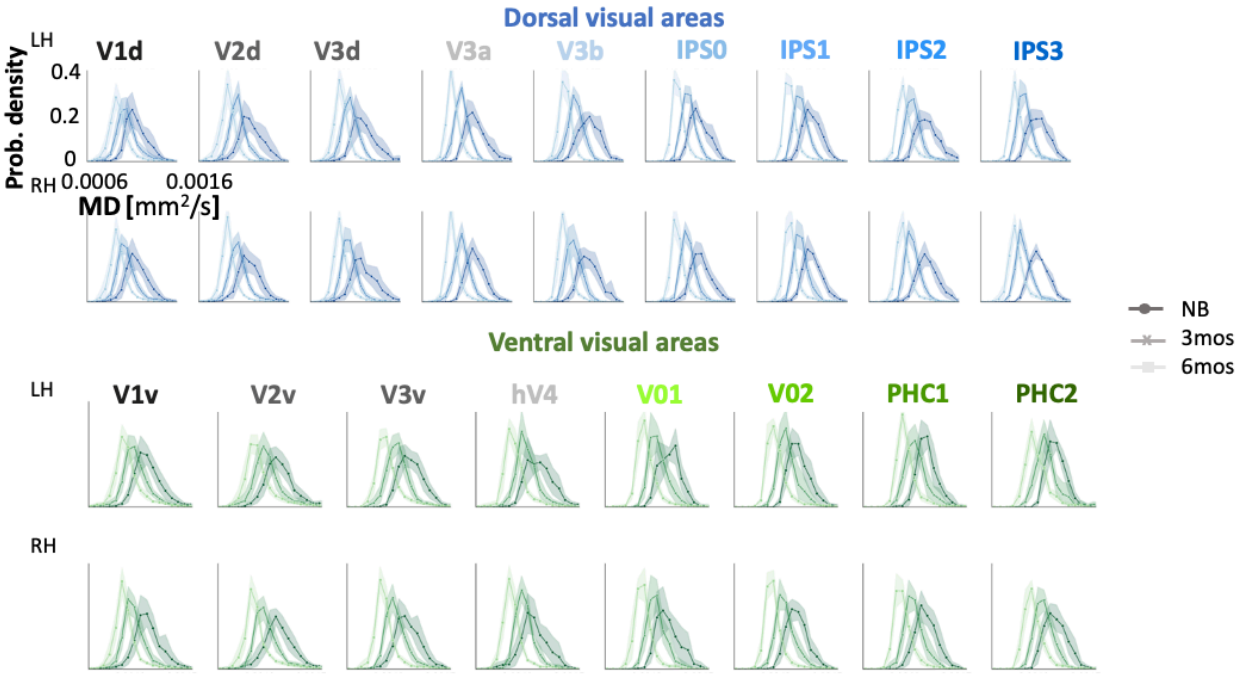

Supplementary Figure 7. Distributions of MD in dorsal and ventral visual regions in the left and right hemisphere in newborns (NB), 3-month-olds (3mos) and 6-month-olds (6mo). Distributions shift leftward with age in the first six months of infant life indicating the MD systematically decreases. *LH/RH: left/right hemisphere. Lines: mean; Shaded areas: SE of the mean across 10 participants per time point.*

Supplementary Table S1. Timepoints completed by infants included in the study. *Green*: scanned, *white:* missing timepoint.

Participant	Birth sex	0 month	3 months	6 months
S1	Male			
S2	Male			
S3	Female			
S4	Female			
S5	Male			
S6	Female			
S7	Male			
S8	Female			
S9	Male			
S10	Female			
S11	Male			
S12	Female			
S13	Male			

Supplementary Table S2. Statistical significance and parameters of linear mixed models (LMMs) quantifying the relationship between mean T_1 and age in primary sensory cortices (related to **Figs. 1** and **S3**). *LH/RH:* left/right hemisphere; *Corr Coeff:* Correlation Coefficient. All values survive Bonferroni correction P<0.001. Slope units: [sec]/age in days

Primary Sensory Regions	***Slope (LH)***	***R* corr coeff (LH)**	***P*-value (LH)**	***Slope (RH)***	***R* corr coeff (RH)**	***P*-value (RH)**
Primary Visual (V1)	-0.0019	-0.86	1.48x10-9	-0.0020	-0.89	2.22x10-11
Primary Auditory (A1)	-0.0013	-0.80	1.33x10-7	-0.0017	-0.85	2.63x10-9
Primary Somatosensory (S1)	-0.0018	-0.91	2.44x10-12	-0.0020	-0.90	9.67x10-12
Primary Motor (M1)	-0.0019	-0.92	8.86x10-13	-0.0019	-0.87	3.73x10-10

Supplementary Table S3. Statistical significance and parameters of LMMs quantifying the relationship between mean MD and age in primary sensory-motor cortices (related to **Fig. S4**). *LH/RH:* left/right hemisphere; *Corr Coeff:* Correlation Coefficient. All values survive Bonferroni correction P<0.001, except those in gray. Slope units: [mm²/sec]/age in days.

Primary Sensory Regions	***Slope (LH)***	***R* corr coeff (LH)**	***P*-value (LH)**	***Slope (RH)***	***R* corr coeff (RH)**	***P*-value (RH)**
Primary Visual (V1)	-1.01x10-6	-0.82	6.13x10-8	-1.08x10-6	-0.87	9.86x10-10
Primary Auditory (A1)	-5.70x10-7	-0.44	0.01	-7.09x10-7	-0.55	0.002
Primary Somatosensory (S1)	-6.40x10-7	-0.58	0.001	-5.48x10-7	-0.60	0.0007
Primary Motor (M1)	-9.36x10-7	-0.78	8.26x10-7	-1.06x10-6	-0.70	2.59x10-5

Supplementary Table S4. Statistical significance and parameters of LMMs quantifying the relationship between mean T_1 and age in dorsal and ventral visual areas (related to **Figs. 2** and **S5**). *LH/RH:* left/right hemisphere; *Corr Coeff:* Correlation Coefficient. All values survive Bonferroni correction P<0.001. Slope units: [sec]/age in days.

Dorsal Regions	***Slope (LH)***	***R* corr coeff (LH)**	***P*-value (LH)**	***Slope (RH)***	***R* corr coeff (RH)**	***P*-value (RH)**
V1d	-0.0020	-0.77	5.70x10-7	-0.0020	-0.82	2.80x10-8
V2d	-0.0023	-0.72	7.45x10-6	-0.0023	-0.82	2.66x10-8
V3d	-0.0026	-0.83	1.08x10-8	-0.0027	-0.85	1.94x10-9
V3a	-0.0027	-0.88	9.26x10-11	-0.0027	-0.89	1.00x10-10
V3b	-0.0023	-0.88	9.14x10-11	-0.0029	-0.91	8.68x10-13
IPS0	-0.0029	-0.89	1.95x10-11	-0.0029	-0.90	1.31x10-11
IPS1	-0.0028	-0.90	7.79x10-12	-0.0030	-0.94	3.58x10-15
IPS2	-0.0026	-0.89	1.71x10-11	-0.0025	-0.91	1.90x10-12
IPS3	-0.0025	-0.93	1.68x10-14	-0.0025	-0.89	3.34x10-11

Ventral Regions	***Slope (LH)***	***R* corr coeff (LH)**	***P*-value (LH)**	***Slope (RH)***	***R* corr coeff (RH)**	***P*-value (RH)**
V1v	-0.0015	-0.73	3.75x10-6	-0.0019	-0.83	8.11x10-9
V2v	-0.0022	-0.83	1.25x10-8	-0.0021	-0.83	8.06x10-9
V3v	-0.0026	-0.85	1.53x10-9	-0.0024	-0.89	2.02x10-11
hV4	-0.0026	-0.81	5.02x10-8	-0.0024	-0.87	2.86x10-10
V01	-0.0027	-0.84	4.81x10-9	-0.0027	-0.91	2.28x10-12
V02	-0.0027	-0.92	4.09x10-13	-0.0028	-0.94	8.50x10-15
PHC1	-0.0025	-0.87	1.59x10-10	-0.0026	-0.92	2.28x10-13
PHC2	-0.0023	-0.82	1.49x10-8	-0.0025	-0.89	3.62x10-10

Supplementary Table 5. Statistical significance and parameters of LMMs quantifying the relationship between mean MD and age in dorsal and ventral visual areas (related to **Figs. 2** and **S6**). *LH/RH:* left/right hemisphere; *Corr Coeff: Correlation Coefficient.* All values survive Bonferroni correction P<0.001. Slope units: [mm²/sec]/age in days.

Dorsal Regions	***Slope (LH)***	***R* corr coeff (LH)**	***P*-value (LH)**	***Slope (RH)***	***R* corr coeff (RH)**	***P*-value (RH)**
V1d	-1.20x10-6	-0.76	1.90x10-6	-1.17x10-6	-0.85	1.01x10-8
V2d	-1.65x10-6	-0.88	3.30x10-10	-1.45x10-6	-0.90	3.19x10-11
V3d	-1.63x10-6	-0.85	1.02x10-8	-1.61x10-6	-0.85	8.85x10-9
V3a	-1.55x10-6	-0.87	6.94x10-10	-1.60x10-6	-0.90	3.41x10-11
V3b	-1.62x10-6	-0.91	1.15x10-11	-1.66x10-6	-0.89	7.67x10-11
IPS0	-1.52x10-6	-0.94	8.84x10-14	-1.63x10-6	-0.90	5.00x10-11
IPS1	-1.67x10-6	-0.91	1.42x10-11	-1.62x10-6	-0.93	7.06x10-13
IPS2	-1.66x10-6	-0.86	2.88x10-9	-1.70x10-6	-0.88	2.35x10-10
IPS3	-1.33x10-6	-0.83	3.89x10-8	-1.43x10-6	-0.89	1.65x10-10

Ventral Regions	***Slope (LH)***	***R* corr coeff (LH)**	***P*-value (LH)**	***Slope (RH)***	***R* corr coeff (RH)**	***P*-value (RH)**
V1v	-1.08x10-6	-0.79	3.40x10-7	-1.14x10-6	-0.80	2.92x10-7
V2v	-1.20x10-6	-0.68	6.18x10-5	-9.81x10-7	-0.63	0.00025
V3v	-1.18x10-6	-0.83	4.57x10-8	-1.07x10-6	-0.81	1.25x10-7
hV4	-1.24x10-6	-0.82	7.17x10-8	-1.10x10-6	-0.80	2.07x10-7
V01	-1.23x10-6	-0.87	1.47x10-9	-1.33x10-6	-0.88	5.91x10-10
V02	-1.17x10-6	-0.87	1.37x10-9	-1.27x10-6	-0.91	6.01x10-12
PHC1	-1.06x10-6	-0.82	8.55x10-8	-1.29x10-6	-0.90	5.13x10-11
PHC2	-1.01x10-6	-0.79	4.53x10-7	-1.21x10-6	-0.85	5.74x10-9

Supplementary Table 6. Demographic information of postmortem human brain tissue samples used for the transcriptomic gene analysis. The data is from the Brain Span Atlas portal at www.brainspan.org. Developmental stages from mid to late prenatal to early infancy were used for the differential gene analysis. *PCW:* post conceptual weeks, *M:* months; *F/M:* female/male; *E* = European, *A* = African American, *H* = Hispanic.

Subject ID	Age at Death	Gender	Ethnicity
	Prenatal samples (in PCW)		
H376.IV.53	19	F	H
H376.IV.51	21	F	E
H376.IV.54	21	M	A
H376.IV.50	22	M	E
H376.V.51	25	F	H
H376.V.52	26	F	A
H376.V.53	37	M	E
	Postnatal samples (in M)		
H376.VI.50	4	M	E
H376.VI.51	4	M	E
H376.VI.52	4	M	A

Supplementary Table 7. Brain regions used for the transcriptomic gene analysis. Tissue samples from prenatal and postnatal human primary sensory-motor, temporal, and parietal cortices profiled by RNA sequencing. Primary motor cortex (M1, BA4), Primary visual cortex (V1, BA17), Primary somatosensory cortex (S1, BA1-3), Primary auditory temporal cortex (A1, BA41), Posterior inferior parietal cortex (IPC, BA40), Posterior superior temporal cortex (STC, BA22), Inferior temporal cortex (ITC, BA20); *PCW*: post conceptual weeks, *M:* months.

Subject ID	Age	Regions
H376.IV.53	19 pcw	M1C-S1C
H376.IV.53	19 pcw	IPC
H376.IV.53	19 pcw	A1C
H376.IV.53	19 pcw	STC
H376.IV.53	19 pcw	V1C
H376.IV.51	21 pcw	ITC
H376.IV.54	21 pcw	M1C
H376.IV.54	21 pcw	S1C
H376.IV.54	21 pcw	IPC
H376.IV.54	21 pcw	STC
H376.IV.54	21 pcw	ITC
H376.IV.54	21 pcw	V1C
H376.IV.50	22 pcw	M1C
H376.IV.50	22 pcw	S1C
H376.IV.50	22 pcw	IPC
H376.IV.50	22 pcw	A1C
H376.IV.50	22 pcw	STC
H376.IV.50	22 pcw	ITC
H376.IV.50	22 pcw	V1C
H376.V.51	25 pcw	A1C
H376.V.52	26 pcw	V1C
H376.V.52	26 pcw	STC
H376.V.53	37 pcw	M1C
H376.V.53	37 pcw	S1C
H376.V.53	37 pcw	IPC
H376.V.53	37 pcw	A1C
H376.V.53	37 pcw	STC
H376.V.53	37 pcw	ITC
H376.V.53	37 pcw	V1C
H376.VI.50	4 M	ITC
H376.VI.50	4 M	STC
H376.VI.50	4 M	V1C
H376.VI.51	4 M	M1C
H376.VI.51	4 M	A1C
H376.VI.51	4 M	STC
H376.VI.51	4 M	ITC
H376.VI.52	4 M	M1C
H376.VI.52	4 M	S1C
H376.VI.52	4 M	IPC
H376.VI.52	4 M	A1C
H376.VI.52	4 M	STC
H376.VI.52	4 M	V1C
H376.VI.52	4 M	ITC

Supplementary Table 8. The gene ontology (GO) list related to Figure 3C. This GO list includes the information on the biological processes related to the 95 most differentially expressed genes, listed by statistical significance of functional enrichment analysis. Complete gene ontology lists without and with background gene sets can be found on GitHub: https://github.com/VPNL/babies_graymatter/genes/Dataset1 and https://github.com/VPNL/babies_graymatter/genes/Dataset2

Category	ID	Name	p-value FDR
GO: Molecular Function	GO:0019911	structural constituent of myelin sheath	2.05E-05
GO: Molecular Function	GO:0042165	neurotransmitter binding	5.57E-04
GO: Biological Process	GO:0098916	anterograde trans-synaptic signaling	1.29E-12
GO: Biological Process	GO:0007268	chemical synaptic transmission	1.29E-12
GO: Biological Process	GO:0099537	trans-synaptic signaling	1.29E-12
GO: Biological Process	GO:0099536	synaptic signaling	1.34E-12
GO: Biological Process	GO:0007267	cell-cell signaling	5.19E-12
GO: Biological Process	GO:0050804	modulation of chemical synaptic transmission	5.82E-08
GO: Biological Process	GO:0099177	regulation of trans-synaptic signaling	5.82E-08
GO: Biological Process	GO:0048167	regulation of synaptic plasticity	2.89E-05
GO: Biological Process	GO:0048666	neuron development	3.56E-05
GO: Biological Process	GO:1900449	regulation of glutamate receptor signaling pathway	3.56E-05
GO: Biological Process	GO:0030030	cell projection organization	6.34E-05
GO: Biological Process	GO:0030182	neuron differentiation	1.02E-04
GO: Biological Process	GO:0042552	myelination	1.38E-04
GO: Biological Process	GO:0032291	axon ensheathment in central nervous system	1.38E-04
GO: Biological Process	GO:0022010	central nervous system myelination	1.38E-04
GO: Biological Process	GO:0008366	axon ensheathment	1.38E-04
GO: Biological Process	GO:0007272	ensheathment of neurons	1.38E-04
GO: Cellular Component	GO:0043005	neuron projection	2.98E-15
GO: Cellular Component	GO:0030424	axon	2.10E-14
GO: Cellular Component	GO:0036477	somatodendritic compartment	1.16E-11
GO: Cellular Component	GO:0045202	synapse	9.90E-10
GO: Cellular Component	GO:0043025	neuronal cell body	1.23E-09
GO: Cellular Component	GO:0044297	cell body	7.07E-09
GO: Cellular Component	GO:0098794	postsynapse	3.81E-07
GO: Cellular Component	GO:0044304	main axon	1.37E-06
GO: Cellular Component	GO:0098793	presynapse	1.02E-05
GO: Cellular Component	GO:0097060	synaptic membrane	2.76E-05
GO: Cellular Component	GO:0030425	dendrite	2.78E-05
GO: Cellular Component	GO:0097447	dendritic tree	2.78E-05